

# Fluctuations in the IRAS 1.2 Jy Catalogue

Martin Kerscher<sup>1</sup>, Jens Schmalzing<sup>1,2</sup>, Thomas Buchert<sup>1</sup>, and Herbert Wagner<sup>1\*</sup>

<sup>1</sup> Ludwig-Maximilians-Universität, Theresienstraße 37, 80333 München, Germany

<sup>2</sup> Max-Planck-Institut für Astrophysik, Karl-Schwarzschild-Straße 1, 85740 Garching, Germany

Received 6 October 1997 / Accepted 23 December 1997

**Abstract.** An analysis of the IRAS 1.2 Jy redshift catalogue with emphasis on the separate examination of northern and southern parts (in galactic coordinates) is performed using a complete set of morphological descriptors (Minkowski functionals), nearest neighbour distributions and the variance of the galaxy counts. We find large fluctuations in the clustering properties as seen in a large difference between the northern and southern parts of the catalogue on scales of  $100h^{-1}\text{Mpc}$ . These fluctuations remain discernible even on the scale of  $200h^{-1}\text{Mpc}$ . We also identify sparse sampling as a major source of “apparent homogenization”. Tests on observational selection effects concerning luminosity, colour and redshift-space distortion support the significance of these large-scale fluctuations.

**Key words:** Cosmology: large-scale structure of the Universe – theory – observations – Galaxies: clustering

## 1. Introduction

The spatial distribution of luminous matter seen in the available galaxy redshift catalogues conveys a complex picture of voids, isolated galaxies, clusters and superclusters, with the largest filamentary features extending on scales comparable with the size of the surveys. Since these findings are expected to provide important constraints for theoretical models of structure evolution, a prime task is to extract the morphological characteristics of the observed patterns by appropriate quantitative measures.

In the present paper we consider the IRAS 1.2 Jy catalogue (Fisher et al. 1995). This infrared-selected survey consists of two data sets for the northern and southern caps (in galactic coordinates) separated by a 10 degree wide zone of avoidance and is therefore nearly all-sky. We analyze the two subsamples individually with Minkowski functionals (Mecke et al. 1994) in order to quantify the

global geometrical and topological features of spatial patterns. In addition, we apply a novel method of cluster diagnostics (van Lieshout and Baddeley 1996) combining local and global statistical descriptors, and the more conventional count-in-cell method.

Practically, when analyzing galaxy surveys one has to deal with various technical problems. As a rule, three-dimensional galaxy catalogues are constructed from redshift surveys which suffer from distortions due to peculiar motions. To date, there is no way of tackling this problem without making strong assumptions (e.g. linearized equations of motion), and therefore we conduct our analysis in redshift space and investigate the differences to real space by comparing with results of  $N$ -body simulations. Furthermore, surveys are usually flux limited. Therefore, the observed number density of the galaxies decreases with distance. For samples with inhomogeneous mean number density the methods employing morphological estimators are usually dominated by thinning at the fringes. One remedy is to focus on volume limited subsamples, at the cost of losing a substantial fraction of galaxies. Nevertheless, we show that Minkowski functionals provide significant results even for a small number of galaxies. Finally, all surveys are spatially limited both in directions as well as in depth, where volume limitation leads to a well-defined spherical boundary. Hence, we have to take care of boundary constraints. In Appendix A we discuss these finite size effects on the estimators for the Minkowski functionals, for the nearest-neighbour distribution, and for the fluctuations of the galaxy counts.

As a result we detect a significant morphological segregation between the northern and the southern part of the IRAS catalogue. These findings are also supported by our further results on the variances of counts in cells, done separately for the north and the south.

## 2. Methods of morphological analysis

We consider a set  $X = \{\mathbf{x}_i\}_{i=1}^N$  of  $N$  points  $\mathbf{x}_i \in \mathbb{R}^3$  given by the redshift-space coordinates of the galaxies in the IRAS 1.2 Jy catalogue (Fisher et al. 1995).

*Send offprint requests to:* T. Buchert

\* emails: kerscher, jens, buchert, wagner@stat.physik.uni-muenchen.de

**Table 1.** Minkowski functionals in three-dimensional space expressed in terms of more familiar geometric quantities.

| geometric quantity          | $\mu$ | $M_\mu$        | $\Phi_\mu$                  |
|-----------------------------|-------|----------------|-----------------------------|
| $V$ volume                  | 0     | $V$            | $V/( \frac{4\pi}{3} r^3 N)$ |
| $A$ surface                 | 1     | $A/8$          | $A/(4\pi r^2 N)$            |
| $H$ integral mean curvature | 2     | $H/(2\pi^2)$   | $H/(4\pi r N)$              |
| $\chi$ Euler characteristic | 3     | $3\chi/(4\pi)$ | $\chi/N$                    |

### 2.1. Minkowski functionals

A computationally convenient and robust method for quantifying the morphology of spatial patterns is offered by Minkowski functionals as they were introduced into cosmology by Mecke et al. (1994). For this purpose we decorate each point  $\mathbf{x}_i$  with a ball  $\mathcal{B}_r(\mathbf{x}_i)$  of radius  $r$  and then consider the union set  $\mathcal{A}_N(r) = \bigcup_{i=0}^N \mathcal{B}_r(\mathbf{x}_i)$ . Hadwiger (1957) proved that in three dimensions the four Minkowski functionals  $M_{\mu=0,1,2,3}(\mathcal{A}_N(r))$  give a complete morphological characterization of a body  $\mathcal{A}_N(r)$ . The interpretation of these functionals in terms of geometrical and topological quantities is given in Table (1).

By normalizing with the functional  $M_\mu(\mathcal{B}_r)$  of a single ball we can introduce normalized, dimensionless Minkowski functionals  $\Phi_\mu(\mathcal{A}_N(r))$ ,

$$\Phi_\mu(\mathcal{A}_N(r)) := \frac{M_\mu(\mathcal{A}_N(r))}{NM_\mu(\mathcal{B}_r)}. \quad (1)$$

In the case of a Poisson process the exact mean values of the functionals can be calculated analytically (Mecke and Wagner 1991). For decorating spheres with radius  $r$  one obtains:

$$\begin{aligned} \Phi_0^P &= (1 - e^{-\eta}) \eta^{-1}, \\ \Phi_1^P &= e^{-\eta}, \\ \Phi_2^P &= e^{-\eta} (1 - \frac{3\pi^2}{32}\eta), \\ \Phi_3^P &= e^{-\eta} (1 - 3\eta + \frac{3\pi^2}{32}\eta^2), \end{aligned} \quad (2)$$

with the dimensionless parameter  $\eta = \bar{n}M_0(\mathcal{B}_r) = \bar{n}4\pi r^3/3$ , where  $\bar{n}$  denotes the mean number density.

For  $\mu \geq 1$  the measures  $\Phi_\mu(\mathcal{A}_N(r))$  contain the exponentially decreasing factor  $e^{-\eta(r)}$ . It can be shown that this exponential decrease with increasing (diagnostic) radius  $r$  also arises for more general cluster processes. Therefore we employ the reduction

$$\phi_\mu(\mathcal{A}_N(r)) = \frac{\Phi_\mu(\mathcal{A}_N(r))}{\Phi_1^P(\mathcal{A}_N(r))}, \quad \mu \geq 1, \quad (3)$$

and thereby remove the exponential decay and enhance the visibility of differences in the displays shown below.

### 2.2. Nearest neighbour statistics

The nearest neighbour distribution  $G(r)$  is a standard tool in the analysis of point processes (Ripley 1988) and is defined as the *distribution of distances  $r$  of a point of the process to the nearest other point of the process*. The function  $G(r)$  is related to conditional correlation functions (White 1979). Another common statistical descriptor is the empty space function  $F(r)$ , the *distribution of the distances  $r$  of an arbitrary point to the nearest point of the process*, and is equal to the expected fraction of volume occupied by points which are less distant than  $r$  from the next point of the process. Therefore,  $F(r)$  is equal to the volume density of  $M_0(\mathcal{A}_N(r))$ ; hence  $1 - F(r)$  coincides with the void probability function  $P_0(r)$  (White 1979). Alternatively, one may interpret  $F(r)$  as the unconditional and  $G(r)$  as the conditional distribution of the nearest neighbour distance. Recently, van Lieshout and Baddeley (1996) advocated to use the ratio

$$J(r) := \frac{1 - G(r)}{1 - F(r)} \quad (4)$$

as a probe for clustering of a point process. In the case of a Poisson process,

$$G^P(r) = 1 - \exp(-\eta) = F^P(r), \quad (5)$$

and thus  $J^P(r) = 1$ . For a process with enhanced clumping, we have  $J(r) < 1$ , whereas regular structures are indicated by  $J(r) > 1$ .

### 2.3. Fluctuations of the galaxy counts

Another frequently used method for exploring galaxy catalogues is to consider the fluctuations of galaxy counts, in particular, the variance of counts in cells in excess of Poisson,

$$\langle (N_i - \bar{n}V)^2 \rangle = \bar{n}V + \bar{n}^2V^2\sigma^2, \quad (6)$$

where  $N_i$  is the number of galaxies in a volume  $V$ , in our case a ball  $\mathcal{B}_r$  with radius  $r$ ; the averaging is performed over random positions of the balls. For a Poisson process,  $\sigma^2 = 0$  by definition. For stationary point processes the variance  $\sigma^2$  is related to the two-point correlation function  $\xi(r)$ ,

$$\sigma^2 = \frac{1}{V^2} \int_V \int_V d^3x d^3y \xi(|x - y|). \quad (7)$$

After averaging a power-law correlation function  $\xi(r) = (r_0/r)^\gamma$  over balls  $\mathcal{B}_r$  one obtains (Peebles 1993):

$$\sigma^2(r) = \left(\frac{r_0}{2r}\right)^\gamma \frac{1}{(1 - \gamma/3)(1 - \gamma/4)(1 - \gamma/6)}. \quad (8)$$

In Appendix B we discuss the dependence of the variance  $\sigma^2$  on the mean number density and we point out how this has to be modified for fractal sets.

### 3. Results

We now apply the methods introduced above to explore a redshift catalogue of 5313 IRAS selected galaxies with limiting flux of 1.2 Jy (Fisher et al. 1995).

#### 3.1. Volume limited samples with $100h^{-1}\text{Mpc}$ depth

A volume limited sample of  $100h^{-1}\text{Mpc}$  depth (with  $h$  defined by  $H_0 = 100h \text{ km s}^{-1} \text{ Mpc}^{-1}$ ) contains 352 galaxies in the northern part, and 358 galaxies in the southern part. In Fig. 1 we see that the redshift and flux distributions of the galaxies do not indicate any peculiarity or problem with the sample. As far as the number density, i.e. the first moment of the galaxy distribution is concerned, the sample does not reveal differences between north and south. However, we want to assess the clustering properties of the data and, above all, tackle the question whether the southern and northern parts differ or not. More refined measurement of the galaxy distribution need to incorporate at least the second moment (see Sect. 3.1.5, 3.2.2). A complete characterization of morphology, depending on all moments of the distribution, is even more desirable. It is provided by the Minkowski functionals.

##### 3.1.1. Minkowski functionals

In Fig. 2 we show the values of the Minkowski functionals of the southern and northern parts, together with the values from a Poisson process with the same number density (the volume density is shown in Fig. 6). The errors for the Poisson process were calculated using twenty different realizations. This already gives a stable estimate of the ensemble variance. To estimate the error for the catalogue data we calculated the Minkowski functionals of twenty subsamples containing 90% of the galaxies, randomly chosen from the volume limited subsample.

In both parts of the 1.2 Jy catalogue the clustering of galaxies on scales up to  $10h^{-1}\text{Mpc}$  is clearly stronger than in the case of a Poisson process, as inferred from the lower values of the functionals for the surface area,  $\phi_1$ , the integral mean curvature,  $\phi_2$ , and the Euler characteristic,  $\phi_3$ . Moreover, the northern and southern parts differ significantly, with the northern part being less clumpy. The most conspicuous features are the enhanced surface area  $\phi_1$  in the southern part on scales from  $12$  to  $20h^{-1}\text{Mpc}$  and the kink in the integral mean curvature  $\phi_2$  at  $14h^{-1}\text{Mpc}$ . This behavior indicates that dense substructures in the southern part are filled up at this scale (i.e. the balls in these substructures overlap without leaving holes), and is presumably the signature of the Perseus–Pisces supercluster (for a more detailed analysis see Kerscher et al. 1996). On scales from  $15$  to  $20h^{-1}\text{Mpc}$ ,  $\phi_2$ , the value of the integral mean curvature is negative, indicating concave structures. In the southern part the Euler characteristic is still negative in this range; therefore, the structure is domi-

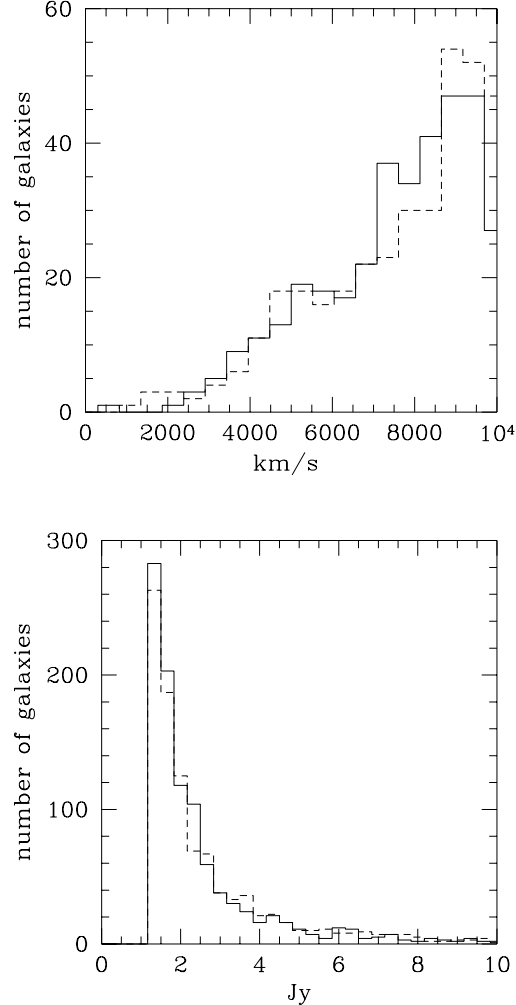


**Fig. 1.** In the top panel we show the histograms of the redshift distribution of the galaxies for the volume limited sample with  $100h^{-1}\text{Mpc}$  depth. In the bottom panel we show the histograms for the flux distribution. The northern part is shown as a solid line, and the southern part as a dashed line.

nated by interconnected tunnels (giving rise to negative contributions to the Euler characteristic) rather than by completely enclosed voids (these would result in positive contributions to the Euler characteristic). A similar feature is seen in the Minkowski functionals of Abell/ACO clusters (Kerscher et al. 1997).

##### 3.1.2. Error estimates

To get an impression how the error from subsampling is related to the intrinsic variance of an ensemble we looked at fixed realizations of a Poisson process within the sample geometry and calculated the error via subsampling using again 90% of the points. This error turns out to be two

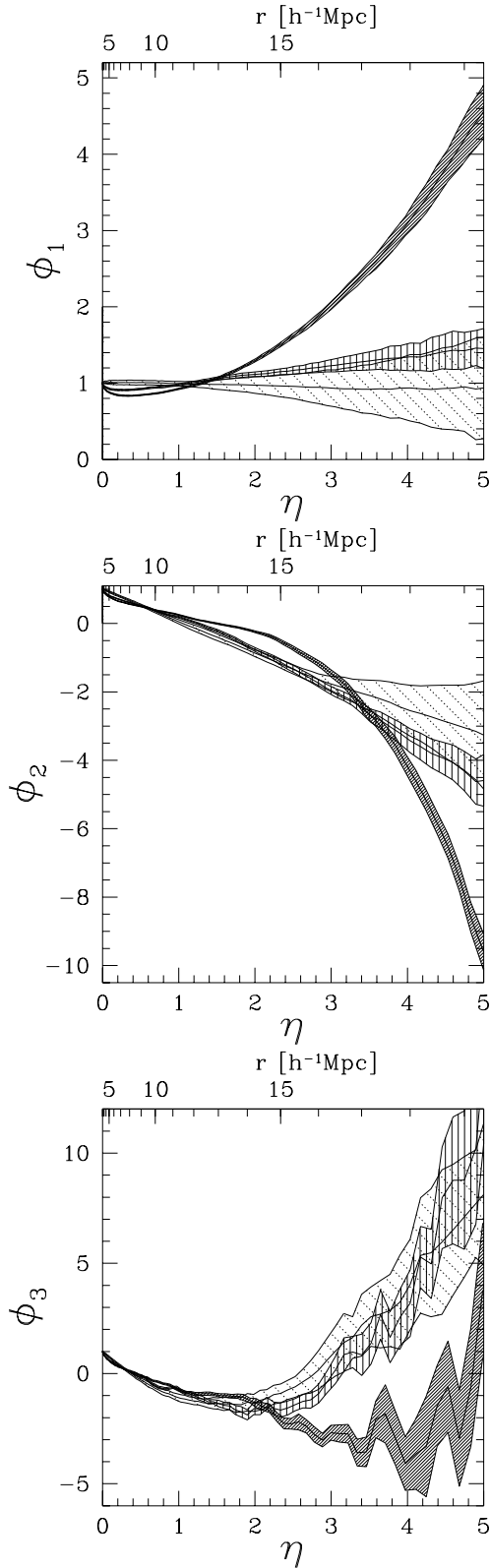


**Fig. 2.** Minkowski functionals  $\phi_\mu$  of a volume limited sample with  $100h^{-1}\text{Mpc}$  depth; the dark shaded areas represent the southern part, the medium shaded the northern part, and the dotted a Poisson process with the same number density. The shaded areas are the  $1\sigma$  errors as explained in the text.

times smaller than the ensemble error calculated over different realizations of a Poisson process.

As for a further error estimate we randomize the redshifts using the quoted redshift errors as the standard deviation (and using the mean redshift error, if none is quoted). These errors are found to be approximately two times smaller than the errors from subsampling as shown in Fig. 2. Even if we increase the quoted redshift error by a factor of five the errors in the functionals are of the same order as determined from subsampling.

In using a window as shown in Fig. A1 we take care of the zone of avoidance. There are additional holes in the redshift catalogue due to a lack of sky coverage or confusion in the point source catalogue. In the northern part these holes account for 3.2% of the catalogue, in the southern part they account for 4.5%. To estimate the influence of these regions on the morphological measures we throw Poisson distributed points with the same number density into these regions. The additional error introduced from these random points is smaller than the error from randomizing the redshifts and therefore, much smaller than the errors from subsampling. Moreover, no systematic effect is seen, the curves overlap completely.

### 3.1.3. Selection effects and the effect of sparse sampling

Several selection effects might enter into the construction of the catalogue. Therefore, we draw subsamples selected according to special features like “colours”, higher limiting flux, and different boundaries.

Before listing these tests we address the important issue of ‘sparse sampling’. This issue is especially relevant for the interpretation of our tests, since all these selected samples incorporate less galaxies than the volume limited sample with  $100h^{-1}\text{Mpc}$  depth. In Fig. 3 we show how sparse sampling affects the surface functionals  $\phi_1(\mathcal{A}_N(r))$  of the volume limited samples with  $100h^{-1}\text{Mpc}$  by only taking a fraction of the galaxies into account (the other functionals behave similarly). By reducing the number of galaxies the error increases and the mean value tends towards the value for a Poisson process. A similar tendency is seen in the sparser volume limited sample with depth  $200h^{-1}\text{Mpc}$  (see Fig. 7).

In view of these findings the following tests were performed:

- We calculated the Minkowski functionals of a volume limited sample with  $100h^{-1}\text{Mpc}$  depth but now with limiting flux equal to 2.0 Jy. Although the noise increases for larger radii, since fewer galaxies enter, the above mentioned features and the difference between northern and southern parts are clearly seen.
- We selected “hot” galaxies, with a flux ratio  $f_{100}/f_{60} \leq 1.5$ , “warm” ones with  $1.5 \leq f_{100}/f_{60} \leq 3$  and “cold” galaxies with  $f_{100}/f_{60} \geq 3$ ;  $f_{100}$  and  $f_{60}$  denote the flux at  $100\mu$  and  $60\mu$ , respectively. We calculated the

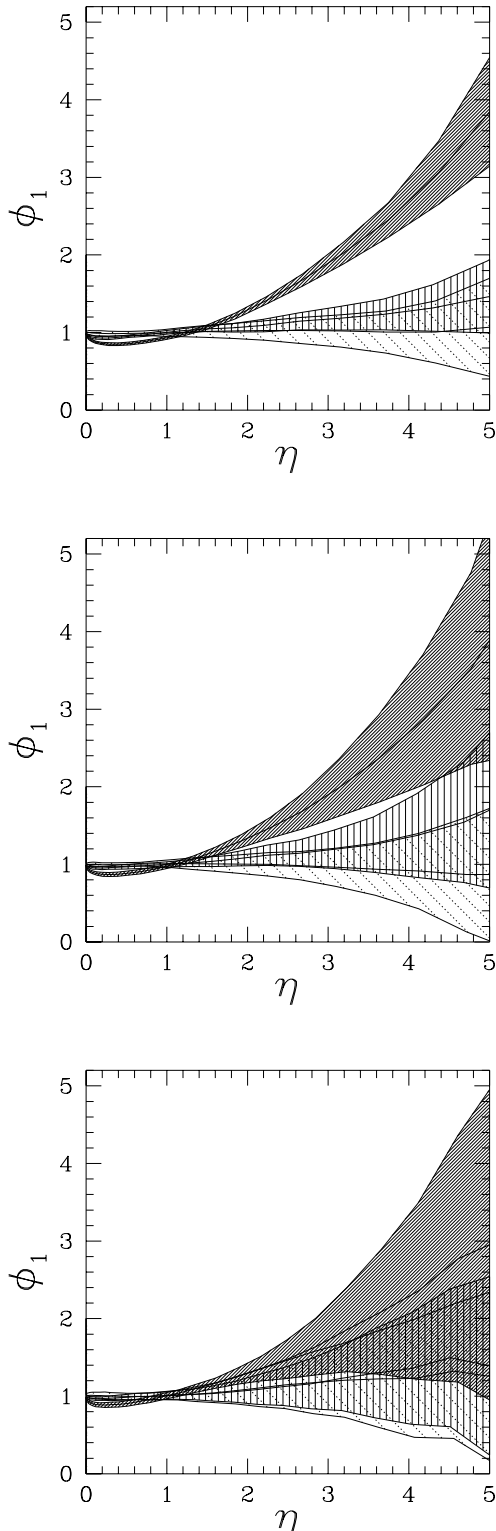


**Fig. 3.** The surface functional  $\phi_1(\mathcal{A}_N(r))$  of a volume limited sample with  $100h^{-1}\text{Mpc}$  depth for randomly drawn subsamples with 70% (top panel), 50% (middle panel), and 30% (bottom panel) galaxies. Again, dark shaded areas represent the southern part, the medium shaded the northern part, and the dotted a Poisson process with the same number density.

Minkowski functionals of volume limited samples with  $100h^{-1}\text{Mpc}$  taken from the “hot” (106 in the north and 116 in the south) and “warm” (239 in the north and 227 in the south) galaxies (only 7 (north) and 15 (south) galaxies are “cold”). Again the error increases, but the distinct features between north and south are still discernible. With similar, but more refined criteria for distinguishing “warm” and “cool” galaxies, Mann et al. (1996) find only a small dependence of clustering on the temperature in the QDOT survey.

- We excluded local structures by looking at galaxies which have a distance from the galactic plane exceeding  $20h^{-1}\text{Mpc}$ . We also changed the window accordingly. The distinct features remain, but the significance decreases.

Therefore, the morphometric difference between the northern and southern parts may not be attributed to luminosity effects, colour effects, or biases due to some peculiar local features.

- By using volume limited subsamples we exclude quite a few galaxies in order to get “clean” samples for a reliable analysis with geometrical estimators. To check this dilution effect we generated a sequence of volume limited samples with limiting depths of  $40h^{-1}\text{Mpc}$ ,  $60h^{-1}\text{Mpc}$ ,  $80h^{-1}\text{Mpc}$ ,  $100h^{-1}\text{Mpc}$ ,  $150h^{-1}\text{Mpc}$ ,  $200h^{-1}\text{Mpc}$ , and  $300h^{-1}\text{Mpc}$ .

Apart from the  $300h^{-1}\text{Mpc}$  sample, which is too strongly diluted to be significant, all these samples show significant differences between the northern and southern parts.

- By cutting the volume limited sample with  $100h^{-1}\text{Mpc}$  depth perpendicular to the galactic plane, we obtain four smaller parts with approximately 160 galaxies each. All four samples show different clustering properties. Therefore, the detected fluctuations cannot be attributed to a special north–south anisotropy.

In Kerscher et al. (1996) we show plots of the Minkowski functionals of the samples incorporating the discussed selection effects.

### 3.1.4. Comparison with a simulation

To generate mock catalogues we use the results of a cosmological simulation (Kolatt et al. 1996) kindly provided by Yair Sigad and Avishai Dekel. The simulation was performed for an  $\Omega = 1$  universe with initial conditions given by a constrained realization of a Gaussian random field. The constraints were calculated from a density field constructed from the IRAS 1.2 Jy galaxy catalogue at present time, evolved backwards in time by inversion of the ‘Zel’dovich approximation’. The simulation forward in time was performed using a particle–mesh code with  $128^3$  particles, each comparable in mass to an average galaxy, in a box with side length  $256h^{-1}\text{Mpc}$ . The purpose of this

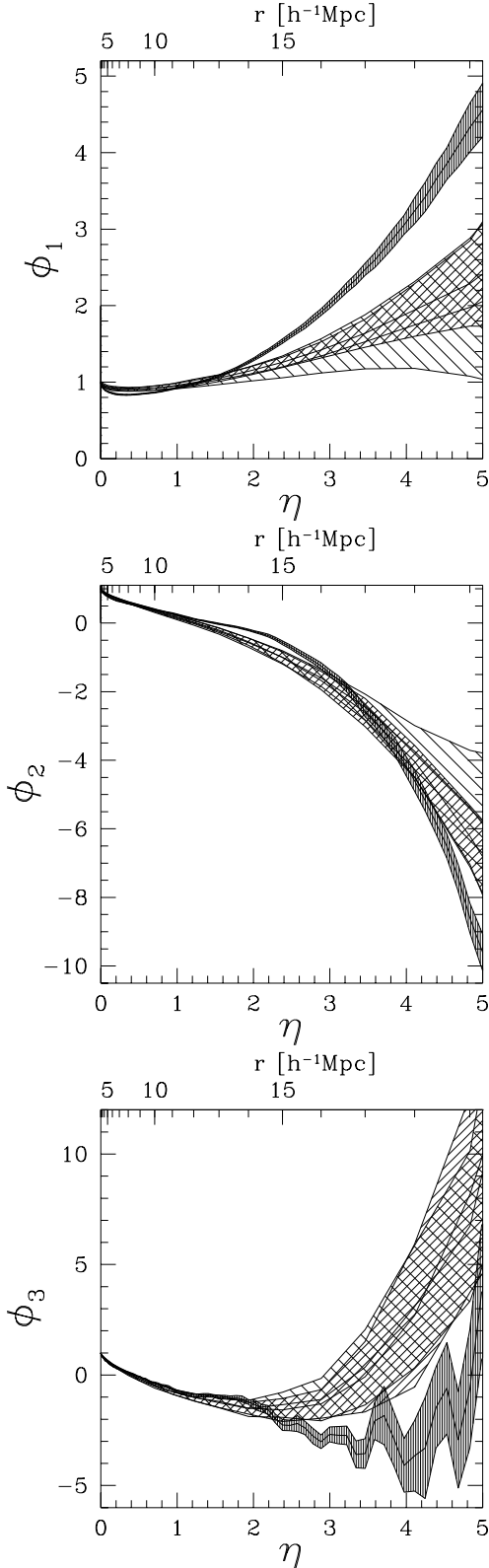


**Fig. 4.** Minkowski functionals  $\phi_\mu$  of a volume limited sample with  $100h^{-1}\text{Mpc}$  depth and of mock samples, southern parts only. The light shaded areas represent the results in redshift-space, the medium shaded the results in real-space, and the dark shaded the results for the IRAS data.

simulation is to mimick the current distribution of matter and to serve as a testcase for statistical methods. We constructed a sequence of twenty mock catalogues both in real- and redshift-space from this simulation by taking only galaxies which are inside the domain of the sample with  $100h^{-1}\text{Mpc}$  depth (see Fig. A1). By randomly selecting these galaxies we make sure to have the same number density as observed in the data. Since we want to compare the morphological properties of the mock samples with the observed galaxy distribution in the northern and southern part separately, we choose the same orientation of the galactic plane as used for the constrained realization of the initial density field.

In Fig. 4 we show the average values of the Minkowski functionals for the southern part of the mock samples both in real- and redshift-space in comparison with the Minkowski functionals of the volume limited observed sample with  $100h^{-1}\text{Mpc}$  depth. For the simulation the error is found by averaging over twenty mock catalogues extracted from the same simulation, for the data we plot the subsampling error. Both results, from real- and redshift-space, are consistent within their errors (the redshift-space results show larger scattering), but they clearly differ from the IRAS data. We attribute this to the small size of the simulation box ( $256h^{-1}\text{Mpc}$  sidelength) compared to the extent of the mock samples ( $200h^{-1}\text{Mpc}$  diameter). The simulation enforces homogeneity on the scale of the sidelength of the box, suppresses fluctuations on that scale, and therefore is not able to reproduce varying clustering properties in distinct regions which nearly fill half of the box each.

Obviously, we demand too much from the simulation which was designed to reproduce the density and velocity fields (and especially their relation) in the nearby region of the universe out to  $60h^{-1}\text{Mpc}$ . In order to cover fluctuations on the scale of  $200h^{-1}\text{Mpc}$ , the simulation simply needs to be significantly larger.

In the case of the northern part the results for the IRAS data and the mock catalogues agree (we do not show them here). The real- and redshift-space results now show the same scattering. The consistency of real- and redshift-space results, both in north and south, gives us confidence that our analysis of the observed IRAS 1.2 Jy catalogue is not affected by redshift space distortions.

### 3.1.5. Nearest neighbour statistics and $\sigma^2$

In Fig. (6) we show the empty space function  $F(r)$ , the nearest neighbour distribution  $G(r)$  and the  $J(r)$  statistics for the volume limited sample with  $100h^{-1}\text{Mpc}$ . The errors are estimated in the same way as for the Minkowski functionals. The error increases with the radius, since  $F$  and  $G$  are approaching unity, and  $(1-G)/(1-F)$  diverges due to random fluctuations.

The volume densities  $F(r)$  differ significantly between north and south. The lowered volume density in the south-

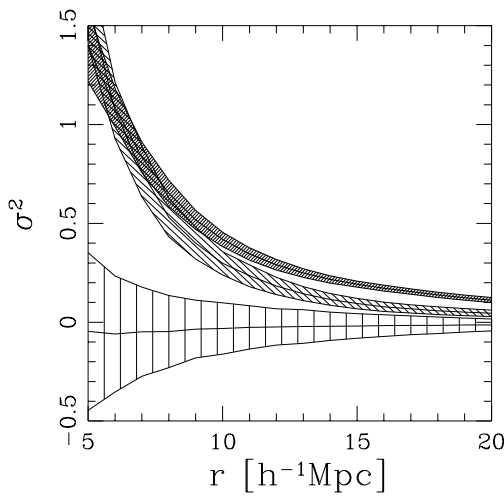


**Fig. 5.**  $\sigma^2$  for the volume limited samples with  $100h^{-1}\text{Mpc}$  depth; again, the dark shaded areas represent the southern part, the medium shaded the northern part, and the light shaded a Poisson process with the same number density.

ern part on scales from  $10$  to  $20h^{-1}\text{Mpc}$  indicates stronger clustering than in the case of a Poisson process, while the northern part is marginally consistent with a Poisson process. The nearest neighbour distributions of the northern and southern parts practically overlap, but differ clearly from the Poisson process. On scales from  $10$  to  $15h^{-1}\text{Mpc}$  the  $J$  statistics discriminates between northern part, southern part and Poisson process, again showing stronger clustering (reduced  $J$ ) in the south.

In Fig. (5) we present the results for the galaxy count fluctuations in a volume limited sample with  $100h^{-1}\text{Mpc}$  depth. On the scale of  $8h^{-1}\text{Mpc}$  both parts display comparable fluctuations of counts in cells with  $\sigma_8 := \sigma(8h^{-1}\text{Mpc}) = 0.81 \pm 0.06$  ( $1\sigma$  error, southern part) and  $\sigma_8 = 0.73 \pm 0.07$  (northern part). These directly measured values both agree with the  $\sigma_8 = 0.77 \pm 0.19$  determined by Fisher et al. (1994) in redshift space, using Eq. (8) and a power-law fit to the correlation function. On larger scales the difference between north and south is clearly seen, as well as their deviation from a Poisson process.

### 3.2. Volume limited samples with $200h^{-1}\text{Mpc}$ depth

To look deeper into space we use a sample which is volume limited to  $200h^{-1}\text{Mpc}$  depth. The northern part then contains 139 galaxies, and the southern part 141 galaxies. The redshift and flux distribution are similar to those shown in Fig. 1.

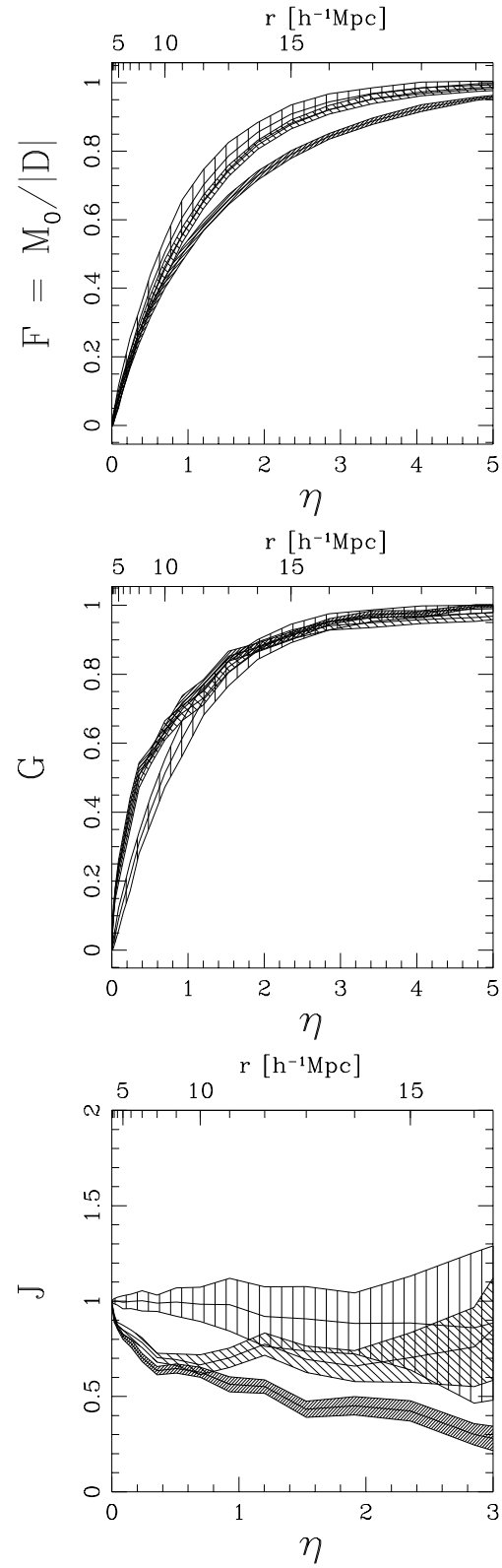


**Fig. 6.**  $F$ ,  $G$  and  $J$  for the volume limited samples with  $100h^{-1}\text{Mpc}$  depth; the dark shaded areas represent the southern part, the medium shaded the northern part, and the light shaded a Poisson process with the same number density.

### 3.2.1. Minkowski functionals

In Fig. 7 the values of the Minkowski functionals of the southern and northern parts are plotted together with the functionals of a Poisson process with the same number density. As before, the errors are determined via subsampling with 90%. Again, the southern part shows a tendency towards stronger clustering, and the enhanced surface area is still clearly detectable, but the overall uncertainty has increased considerably. As pointed out in Sect. 3.1.3 the reduced deviations from the Poisson data should not be attributed to a homogenization of the underlying matter distribution on the scale of  $200h^{-1}\text{Mpc}$ , but rather are due to sparse sampling with only  $\approx 140$  galaxies in each part.

### 3.2.2. Nearest neighbour statistics and $\sigma^2$

The nearest neighbour distribution  $G(r)$  and the  $J(r)$  statistics for the volume limited sample with  $200h^{-1}\text{Mpc}$  depth are shown in Fig. 8. The volume density, the nearest neighbour distribution, and the  $J(r)$  statistics of the northern part are consistent with a Poisson distribution, while the southern part differs in  $G(r)$  and  $J(r)$  both from a Poisson process and from the northern part.

The galaxy count fluctuations (Fig. 9) for a volume limited sample with  $200h^{-1}\text{Mpc}$  depth show clearly a difference between northern and southern parts, but only the southern part deviates from a Poisson process.

Figure 10 presents the average values of  $\sigma^2$  over both parts for volume limits of  $100h^{-1}\text{Mpc}$  and  $200h^{-1}\text{Mpc}$  together with the results of Oliver et al. (1996) and Fisher et al. (1994). For the  $200h^{-1}\text{Mpc}$  sample our averaged values are in good agreement with the results of Oliver et al. (1996); since  $\sigma^2$  differ between the northern and southern parts, the errors quoted by Oliver et al. (1996) are underestimated. This may be a result of their method: These authors calculate  $\sigma^2$  in shells, and use the mean number density *in one shell* in calculating the variance of the count in cells. Hence, they *assume* homogeneity by implicitly weighting with the selection function.

We also plot  $\sigma^2(r)$  according to Eq. (8) with the values  $r_0 = 4.27_{-0.81}^{+0.66}h^{-1}\text{Mpc}$  and  $\gamma = 1.68_{-0.29}^{+0.36}$  as given by Fisher et al. (1994) for the volume limited sample with  $100h^{-1}\text{Mpc}$  depth for both northern and southern parts. These values were determined from a fit to the correlation function in the range from 1 to  $13h^{-1}\text{Mpc}$ . Within the quoted errors our results are consistent with the results of Fisher et al. (1994), with a clear tendency towards lower values of  $\sigma^2$  on larger scales (compared to the  $100h^{-1}\text{Mpc}$  sample).

The  $\sigma^2$  determined from the volume limited samples with  $100h^{-1}\text{Mpc}$  and  $200h^{-1}\text{Mpc}$  differ. This variation of  $\sigma^2$  for the 1.2 Jy data reveals a dependency of  $\sigma^2$  on the mean number density  $\bar{n}$  and on the depth of the samples ( $\bar{n} = 1.84 \times 10^{-4} (h^{-1}\text{Mpc})^{-3}$  for the sample with

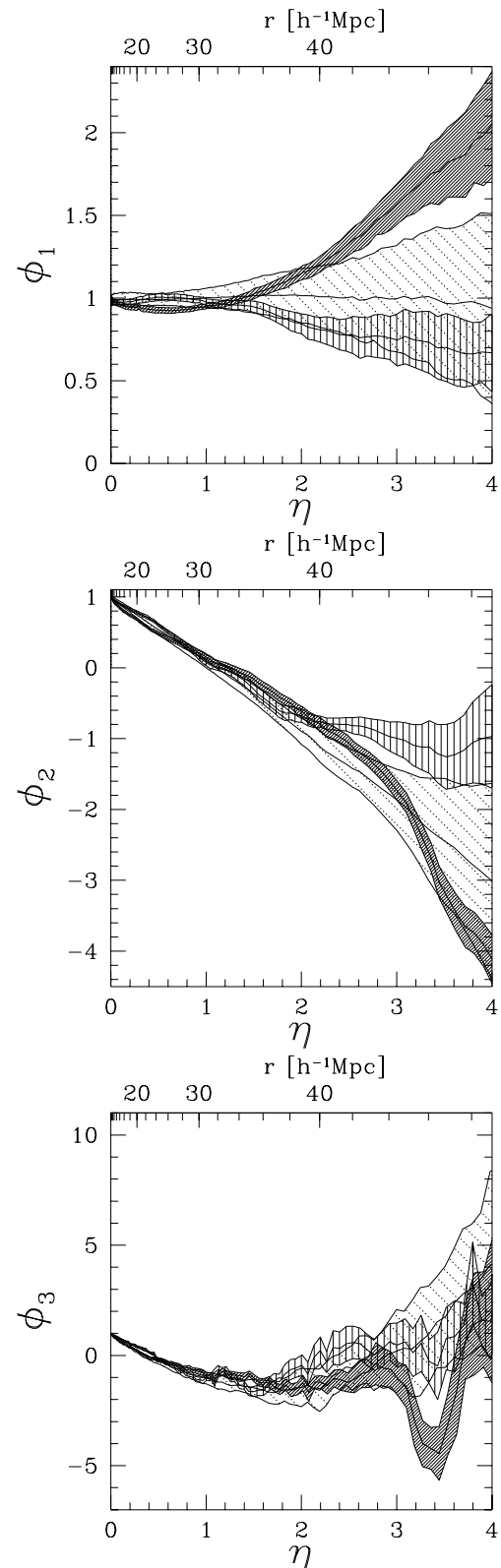


**Fig. 7.** Minkowski functionals  $\phi_\mu(\mathcal{A}_N(r))$  of a volume limited sample with  $200h^{-1}\text{Mpc}$  depth; the dark shaded areas represent the southern part, the medium shaded the northern part, and the light shaded a Poisson process with the same number density.

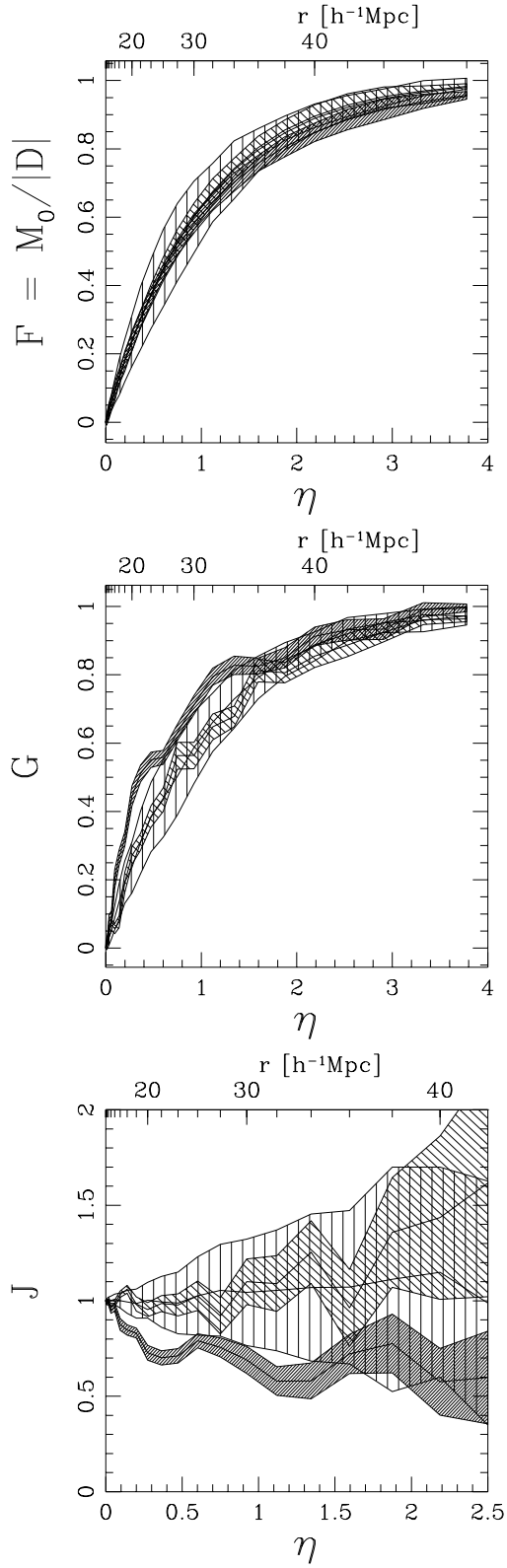


**Fig. 8.**  $F$ ,  $G$  and  $J$  of a volume limited sample with  $200h^{-1}\text{Mpc}$  depth; the dark shaded areas represent the southern part, the medium shaded the northern part, and the light shaded a Poisson process with the same number density.

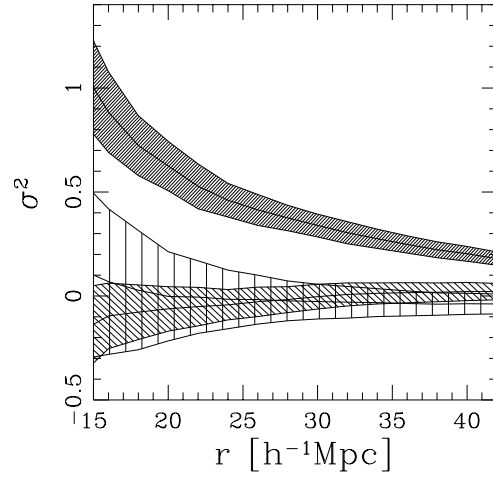


**Fig. 9.**  $\sigma^2$  for the volume limited samples with  $200h^{-1}\text{Mpc}$  depth; again, the dark shaded areas represent the southern part, the medium shaded the northern part, and the light shaded a Poisson process with the same number density.

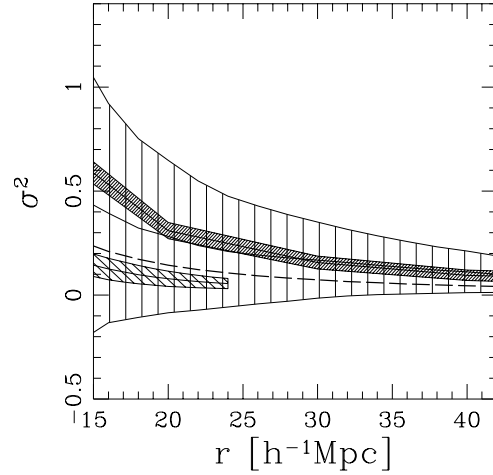


**Fig. 10.** The mean values for  $\sigma^2$  for the volume limited samples with  $100h^{-1}\text{Mpc}$  and  $200h^{-1}\text{Mpc}$  depth; the dark shaded area marks the result of Oliver et al. (1996), the medium shaded the mean result for the  $100h^{-1}\text{Mpc}$  sample, and the light shaded the mean result for the  $200h^{-1}\text{Mpc}$  sample. The dashed line gives the results for  $\sigma^2$  as in Eq. (8) with  $r_0 = 4.27h^{-1}\text{Mpc}$  and  $\gamma = 1.68$  according to Fisher et al. (1994).

$100h^{-1}\text{Mpc}$  depth and  $\bar{n} = 9.05 \times 10^{-6} (h^{-1}\text{Mpc})^{-3}$  for the sample with  $200h^{-1}\text{Mpc}$  depth). In Appendix B we show for a point distribution on a fractal, as a simple still

tractable model, that  $\sigma^2$  depends on the mean number density  $\bar{n}$  and the depth of the sample.

#### 4. Morphometry of a point set

In previous sections, we applied Minkowski functionals as morphological tools to analyze spatial patterns displayed by galaxy catalogue data. Here, we comment on the rationale of this method, which became established only recently in the cosmology literature.

Basically, a galaxy catalogue is a finite set of triple-numbers  $X = \{\mathbf{x}_i\}_{i=1}^N$  representing a skeleton pattern of points imbedded in a domain  $D$  of a three-dimensional Euclidean space. The geometrical information supplied by this skeleton may be organized in a collection of particle distributions,

$$\Gamma_n(\mathbf{y}_1, \dots, \mathbf{y}_n | D), \quad 1 \leq n \leq N, \quad (9)$$

with

$$\begin{aligned} \Gamma_n(\mathbf{y}_1, \dots, \mathbf{y}_n | D) := \\ \sum_{(i_1, \dots, i_n)} \delta(\mathbf{y}_1 - \mathbf{x}_{i_1}) \dots \delta(\mathbf{y}_n - \mathbf{x}_{i_n}), \end{aligned} \quad (10)$$

where the sum runs over all  $n$ -tupels  $(i_1, \dots, i_n)$  with  $1 \leq i_1 < \dots < i_n \leq N$ , and each  $\mathbf{y}_i$  is chosen to lie within  $D$ .

What is the “form” of this point set? Visual inspection habitually conveys the impression of distinct structural features such as clumps, voids, “Great Walls”, “chessboard universe”, or even “Fingers of God”. However, these subjective impressions may be deceptive. To associate a form with a point set, we must put flesh on the skeleton. We have done this in a technically controllable way by covering the points with copies of a ball  $\mathcal{B}_r$  to create a body  $\mathcal{A}_N(r) = \bigcup_{i=0}^N \mathcal{B}_r(\mathbf{x}_i)$ , where the common radius  $r$  may be employed as a variable diagnostic parameter.

The Minkowski functionals are directly related with familiar geometrical and topological quantities (see Table 1) and are ideally suited to measure content, shape, and connectivity of bodies such as  $\mathcal{A}_N(r)$ . In order to explicate their connection with the catalogue data, let us write

$$\mathcal{A}_N(r) = \bigcup_{i=0}^N \mathcal{B}_r(\mathbf{x}_i) = \mathcal{A}_{N-1}(r) \cup \mathcal{B}_r(\mathbf{x}_N). \quad (11)$$

One of the basic properties of the functionals  $M_\mu(\cdot)$  is *additivity* which implies, in particular,

$$\begin{aligned} M_\mu(\mathcal{A}_N(r)) = M_\mu(\mathcal{B}_r(\mathbf{x}_N)) + M_\mu(\mathcal{A}_{N-1}(r)) - \\ M_\mu(\mathcal{A}_{N-1}(r) \cap \mathcal{B}_r(\mathbf{x}_N)). \end{aligned} \quad (12)$$

By iterating Eq. (12), we ultimately arrive at

$$\begin{aligned} M_\mu(\mathcal{A}_N(r)) = \\ \sum_{n=1}^N (-1)^{n-1} \sum_{(i_1, \dots, i_n)} M_\mu(\mathbf{x}_{i_1}, \dots, \mathbf{x}_{i_n}; r), \end{aligned} \quad (13)$$

where we have set  $M_\mu(\mathbf{x}_{i_1}, \dots, \mathbf{x}_{i_n}; r) = M_\mu(\mathcal{B}_r(\mathbf{x}_{i_1}) \cap \dots \cap \mathcal{B}_r(\mathbf{x}_{i_n}))$ . In terms of the particle distribution  $\Gamma_n$ , the expression (13) can be written as

$$\begin{aligned} M_\mu(\mathcal{A}_N(r)) = \sum_{n=1}^N (-1)^{n-1} \int_D d^3x_1 \dots \int_D d^3x_n \\ M_\mu(\mathbf{x}_1, \dots, \mathbf{x}_n; r) \Gamma_n(\mathbf{x}_1, \dots, \mathbf{x}_n | D). \end{aligned} \quad (14)$$

Evidently, the values  $M_\mu(\mathcal{A}_N(r))$  of the Minkowski functionals are determined uniquely by the input data encoded in the distributions  $\Gamma_n$ , once a covering is chosen. Equation (12) remains valid when the balls are replaced by congruent copies of some other compact convex set; however, the values  $M_\mu(\cdot)$  for a given catalogue vary with the choice of the coverage.

We note that the present approach is purely combinatorial; no statistical assumptions enter (beyond those involved in the construction of the sample catalogue), and the problem of “fair samples” does not arise.

Let us compare two samples (1) and (2) with the number of galaxies  $N_1 \approx N_2$  in a common domain. If we find the values of  $M_\mu(\mathcal{A}_{N_1}^{(1)}(r))$  and  $M_\mu(\mathcal{A}_{N_2}^{(2)}(r))$  to differ over some finite range of values of the radius  $r$  then the samples are certainly distinct morphologically. For instance, the V-shaped spike in the normalized Euler characteristic  $\Phi_3$ , seen in Fig. 7, is not a random deviation due to some poor statistics but provides definitive evidence for higher connectivity (i.e. higher genus) of the southern covering body in comparison with the northern one when  $r \approx 46h^{-1}\text{Mpc}$ .

#### 5. Summary and Conclusions

We analyzed morphological characteristics of the galaxy distribution described by the IRAS 1.2 Jy catalogue. The two subsamples (north and south) of this catalogue were studied individually by employing three different methods: (i) Minkowski functionals, (ii) nearest-neighbour distribution, and (iii) variance in the galaxy number counts.

Since the IRAS data have been obtained from a single instrument with uniform calibration, the two subsamples, which contain about the same number of galaxies, can be compared reliably.

To assess the significance of our results we took some care to account for selection and finite size effects. For reference purposes we used typical realizations of a stationary Poisson point process.

Our results may be summarized as follows:

- The values of the Minkowski functionals for the southern part differ significantly from those for the northern part. This morphological segregation is seen in the volume limited subsamples both with  $100h^{-1}\text{Mpc}$  depth and with  $200h^{-1}\text{Mpc}$  depth, but it is less pronounced in the latter case because of sparse sampling. The Minkowski values of the southern part in particular

exhibit drastic deviations from the reference Poisson samples.

- The structural difference between north and south is also clearly detectable both in the nearest-neighbour distribution and in the variance of galaxy number counts. The clustering in the south is recognizably stronger than in the north.

A similar anisotropy in the angular distributions of IRAS galaxies around the northern and southern galactic poles has already been reported by Rowan-Robinson et al. (1986) and was confirmed by Lonsdale et al. (1990). However, the majority of previous IRAS catalogue studies (e.g. Bouchet et al. 1993, Fisher et al. 1994, Kaiser et al. 1991, Oliver et al. 1996, Protogeros and Weinberg 1997, Yess et al. 1997) focused attention on the complete sample without addressing the distinction of its constituent parts.

There is no reason to assume a distinguished position of the Milky Way galaxy; we therefore conclude that fluctuations in the global morphological characteristics of the IRAS sample extend over length-scales of  $200h^{-1}\text{Mpc}$ , at least. These fluctuations may originate from dynamical correlations in the matter distribution which arise during cosmic evolution.

Fluctuations occurring on scales up to  $200h^{-1}\text{Mpc}$ , at least, imply that cosmological simulations which *enforce* homogeneity on the scale of a few hundreds of  $h^{-1}\text{Mpc}$  and suppress fluctuations on larger scales by using periodic boundary conditions cannot reproduce the large-scale fluctuations indicated by the present analysis of the 1.2 Jy catalogue. This assertion is confirmed by our comparison with IRAS mock catalogues drawn from simulations of  $256h^{-1}\text{Mpc}$  box-length.

Recently Davis (1996) used the flux limited 1.2 Jy galaxy catalogue without volume limitation and looked at galaxies in different redshift intervals, projected onto the sphere. He found strong anisotropies in the number density in the nearby region but less in the deeper regions and claims to see a cross-over towards a random homogeneous distribution on scales well below the sample size. However, our results underline that the visual impression of homogeneity on larger scales, especially if based essentially on the number density, is indeed deceptive and misleading.

During the last few years, Pietronero et al. (1996), see also Sylos Labini et al. (1997) or Coleman and Pietronero (1992), have advanced an interpretation of galaxy catalogue data in terms of a fractal support of the galaxy distribution. By its nature, a pure fractal indeed exhibits fluctuations in  $N$ -point distributions on all scales. Our results neither support nor contradict this interpretation, since the Minkowski functionals, as employed in the present paper, are global measures and are not designed to discriminate local structures of spatial patterns.

It will be highly interesting to repeat the present analysis for the upcoming PSCz catalogue, and for an optically selected survey. Forthcoming work will also focus on the

analysis of mock catalogues and cosmic variance in large ( $\gtrsim 1h^{-1}\text{Gpc}$ ) simulations.

## Acknowledgements

We thank Thomas Boller, Stephanie Côté, Luiz da Costa, Avishai Dekel, Vicent Martínez, Maria Jesus Pons-Bordería, Gustav Tammann, Roberto Trasarti-Battistoni, and Simon D.M. White for stimulating discussions. We are grateful to Avishai Dekel and Yair Sigad for kindly providing the simulation. MK and TB acknowledge support from the *Sonderforschungsbereich SFB 375 für Astroteilchenphysik der Deutschen Forschungsgemeinschaft* and from Acciones Integradas during their stay in València where parts of this work were prepared.

The software for calculating the Minkowski functionals, and also the other measures employed, can be obtained by sending email to [buchert@stat.physik.uni-muenchen.de](mailto:buchert@stat.physik.uni-muenchen.de).

## Appendix A: Boundary corrections

This appendix summarizes boundary corrected estimators for the Minkowski functionals  $M_\mu$ , the nearest neighbour distributions  $F$  and  $G$  and for the fluctuations of counts in cells  $\sigma^2$ . All estimators are unbiased only for a statistically “fair” sample and a stationary point process. However, we use identical window geometries for the northern and the southern parts, so we may still compare the two parts without making these assumptions. Moreover the observed discrepancies can be used to falsify at least one of them.

### A.1. Boundary correction for Minkowski functionals

Integral geometry offers a concise way of dealing with contributions of the sample geometry (Mecke and Wagner 1991). In Schmalzing et al. (1996) we discuss a method for completely removing boundary effects.

Let  $D$  be the window, i.e. the sample geometry through which we look at the galaxies. First of all, we must shrink the window  $D$  by the radius  $r$ , otherwise we would miss contributions from balls situated outside the sample (as shown in Fig. A1). The shrunken window is  $D_r := D \cup \mathcal{B}_r$ .

We calculate the Minkowski functionals  $M_\mu(D_r)$  of the window itself, and the Minkowski functionals  $M_\mu(\mathcal{A}_N(r) \cap D_r)$  of the intersection of the window with the union of all balls (see Fig. (A1)). From these numerically measured values, the volume densities  $m_\mu(\mathcal{A}_r)$  of the Minkowski functionals of the union set without the window are ob-

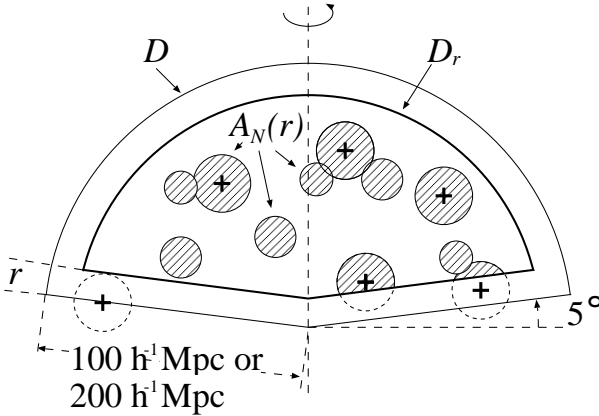


**Fig. A1.** A cut through the union set of balls  $\mathcal{A}_N(r)$ , within the shrunken window  $D_r$ .

tained by the recursive formula<sup>1</sup>

$$m_\mu(\mathcal{A}_N(r)) = \frac{M_\mu(\mathcal{A}_N(r) \cap D_r)}{M_0(D_r)} - \sum_{\nu=0}^{\mu-1} \binom{\mu}{\nu} m_\nu(\mathcal{A}_N(r)) \frac{M_{\mu-\nu}(D_r)}{M_0(D_r)}. \quad (\text{A1})$$

Equation (A1) is just a linear transformation of the functionals  $M_\mu(\mathcal{A}_N(r) \cap D_r)$  calculated for one realization of the point process. Hadwiger's Theorem (Hadwiger 1957) asserts that the  $m_\mu(\mathcal{A}_N(r))$  are a complete set of morphological descriptors equivalent to  $M_\mu(\mathcal{A}_N(r) \cap D_r)$ . What is more, the mean values of  $m_\mu(\mathcal{A}_N(r))$  are analytically known for the Poisson process, and can be directly compared to the results in Eq. (2). Finally, for a fair sample of a stationary point process they are *unbiased estimators* of volume densities of the Minkowski functionals (Fava and Santaló 1978; Fava and Santaló 1979).

#### A.2. Boundary correction for nearest neighbour statistics

Ripley (1988) gives several estimators for  $F$  and  $G$  applicable to spatial point processes with boundaries. In our work we exclusively use the minus estimators (also called reduced sample estimators)  $\widehat{F}$  and  $\widehat{G}$ .

The definition uses the distance  $\rho(\mathbf{y}, X)$  of a point  $\mathbf{y}$  to the nearest point of the pattern  $X = \{\mathbf{x}_i\}_{i=1}^N$ ,

$$\rho(\mathbf{y}, X) := \min(\|\mathbf{x}_i - \mathbf{y}\| \mid \mathbf{x}_i \in X \text{ and } \mathbf{x}_i \neq \mathbf{y}), \quad (\text{A2})$$

and the distance  $\rho(\mathbf{y}, D)$  of a point  $\mathbf{y}$  to the boundary of the window  $D$ ,

$$\rho(\mathbf{y}, D) := \min(\|\mathbf{z} - \mathbf{y}\| \mid \mathbf{z} \notin D). \quad (\text{A3})$$

As explained in Sect. 2.2,  $F(r)$  gives the probability of finding a point of the pattern  $X$  within a distance  $r$  around

<sup>1</sup> We use the convention  $\sum_{i=0}^{-1} a_i = 0$  to include the case  $\mu = 0$ .

a randomly selected point  $\mathbf{y}$ . Therefore we estimate the proportion of points  $\mathbf{y} \in D$  with  $\rho(\mathbf{y}, X) \leq r$ . In order to obtain an unbiased estimator,  $\mathbf{y}$  has to keep a distance of at least  $r$  from the window's boundary, i.e.  $r \leq \rho(\mathbf{y}, D)$ . Therefore, let  $\{\mathbf{y}_j\}_{j=1}^M$  be  $M$  randomly distributed points  $\mathbf{y}_j \in D_r$  inside the shrunken window  $D_r$ . Then  $\widehat{F}(r)$  is defined by

$$\widehat{F}(r) = \frac{\#\{\mathbf{y}_j \mid \rho(\mathbf{y}_j, X) \leq r\}}{M}, \quad (\text{A4})$$

where  $\#\{\dots\}$  gives the number of points in the set  $\{\dots\}$ .

Note that Eq. (A4) is nothing but a Monte Carlo integration of the volume  $\mathcal{A}_N(r) \cap D_r$ . This is a direct consequence of the equality  $F_0(r) = m_0(r)$  mentioned earlier.

To estimate  $G(r)$  we also use a reduced sample estimator (Ripley 1988). Since  $G(r)$  gives the probability of finding another point of the pattern  $X$  within a distance  $r$  around a point  $\mathbf{x} \in X$ , we simply replace the random sample used in Eq. (A4) by the pattern  $X$ . The minus estimator  $\widehat{G}(r)$  is then defined by

$$\widehat{G}(r) = \frac{\#\{\mathbf{x}_j \mid \rho(\mathbf{x}_j, X) \leq r \leq \rho(\mathbf{x}_j, D)\}}{\#\{\mathbf{x}_j \mid r \leq \rho(\mathbf{x}_j, D)\}}. \quad (\text{A5})$$

#### A.3. Boundary correction for galaxy count fluctuations

For estimating  $\sigma^2(r)$  as defined in Eq. (6), we randomly throw two million balls  $\mathcal{B}_r$ , count the number of points in each and calculate the variance. In order to take care of the boundaries we only choose balls lying completely within the window  $D$ . This means their centres have to fall into the shrunken window  $D_r$ .

#### Appendix B: $\sigma^2$ for a fractal, and dependence on $\bar{n}$

Figure 10 reveals differences of  $\sigma^2$  between the  $100h^{-1}\text{Mpc}$  and the  $200h^{-1}\text{Mpc}$  samples. Although some of the results are still consistent given the relatively large errorbars, another explanation of the differences is possible. In this appendix we calculate the dependence of  $\sigma^2$  on the depth  $R_0$  and the number of points  $N_0$  for a sample drawn from a fractal distribution of galaxies.

The generalization of  $\sigma^2$  to point processes on fractal sets is not straightforward, since the mean number density  $\bar{n}$  is not well-defined. In the definition given in Eq. (6) we have to replace the number of points in a ball of radius  $r$  by  $N(r)$  instead of  $\bar{n}V(\mathcal{B}_r)$ , so

$$\sigma^2(r) := \frac{\langle (N_i - N(r))^2 \rangle - N(r)}{N^2(r)} \quad (\text{B1})$$

For a fractal of correlation dimension  $D$  this quantity depends on the radius through

$$N(r) = \left( \frac{N_0}{R_0^D} \right) r^D, \quad (\text{B2})$$

where the constant of normalization  $N_0/R_0^D$  is given for a spherical sample of radius  $R_0$  containing  $N_0$  galaxies. The generalization to cones and an application to number counts is discussed in Sylos Labini et al. (1996). With Eq. (B2) plugged into the definition in Eq. (B1) we obtain

$$\sigma^2(r) = \frac{\langle N_i^2 \rangle}{N_0^2} \left( \frac{R_0}{r} \right)^{2D} - \frac{1}{N_0} \left( \frac{R_0}{r} \right)^D - 1. \quad (\text{B3})$$

Obviously  $\sigma^2$  depends on  $N_0$  and  $R_0$  nontrivially if  $D < 3$ . For a stationary process with  $D = 3$  the average density  $\bar{n} := N_0/V_0 = N_0/(\frac{4\pi}{3}R_0^3)$  is independent of the sample size and we have

$$\sigma^2(r) = \langle N_i^2 \rangle (\bar{n} \frac{4\pi}{3} r^3)^{-2} - (\bar{n} \frac{4\pi}{3} r^3)^{-1} - 1 \quad (\text{B4})$$

as a function of the mean number density  $\bar{n}$ . Since  $\langle \cdot \rangle$  is defined as a volume average,  $\langle N_i^2 \rangle$  determined for one realization may differ from an average over several realizations, i.e. universes. If one assumes ergodicity of the point distribution (implying homogeneity), the volume average converges towards the ensemble average. In this case we get for example for a Poisson process  $\langle N_i^2 \rangle = (\bar{n} \frac{4\pi}{3} r^3)^2 + \bar{n} \frac{4\pi}{3} r^3$  and hence  $\sigma^2(r) = 0$ .

## REFERENCES

Bouchet F. R., Strauss M. A., Davis M. et al., 1993, ApJ 417, 36

Coleman P. H., Pietronero L., 1992, Physics Rep. 213, 311

Davis M.: 1996, *Is the Universe homogeneous on large scales?* In: *Critical Dialogues in Cosmology*, Turok, N. (ed.), astro-ph/9610149

Fava N. A., Santaló L. A., 1978, J. Appl. Prob. 15, 494

Fava N. A., Santaló L. A., 1979, Z. Wahrscheinlichkeitstheorie verw. Gebiete 50, 85

Fisher K. B., Davis M., Strauss M. A. et al., 1994, MNRAS 266, 50

Fisher K. B., Huchra J. P., Strauss M. A. et al., 1995, ApJS 100, 69

Hadwiger H., 1957, *Vorlesungen über Inhalt, Oberfläche und Isoperimetrie*, Springer Verlag, Berlin

Kaiser N., Efstathiou G., Ellis R. et al., 1991, MNRAS 252, 1

Kerscher M., Schmalzing J., Buchert T., Wagner H.: 1996, *The significance of the fluctuations in the IRAS 1.2 Jy galaxy catalogue*. In: *Proc. 2<sup>nd</sup> SFB workshop on Astro-particle physics Ringberg 1996, Report SFB375/P002* (Ringberg, Tegernsee), Bender, R., Buchert, T., Schneider, P. (eds.), p. 83

Kerscher M., Schmalzing J., Retzlaff J. et al., 1997, MNRAS 284, 73

Kolatt T., Dekel A., Ganon G., Willick J. A., 1996, ApJ 458, 419

Lonsdale C. J., Hacking P. B., Conrow T. P., Rowan-Robinson M., 1990, ApJ 358, 60

Mann R. G., Saunders W., Taylor A. N., 1996, MNRAS 279, 636

Mecke K. R., Wagner H., 1991, J. Stat. Phys. 64, 843

Mecke K. R., Buchert T., Wagner H., 1994, A&A 288, 697

Oliver S. J., Rowan-Robinson M., Broadhurst T. J. et al., 1996, MNRAS 280, 673

Peebles P. J. E., 1993, *Principles of physical cosmology*, Princeton University Press, Princeton, New Jersey

Pietronero L., Montuori M., Sylos Labini F.: 1996, *On the fractal structure of the visible Universe*. In: *Critical Dialogues in Cosmology*, Turok, N. (ed.), astro-ph/9611197

Protogeros Z. A. M., Weinberg D. H., 1997, ApJ 489, 457

Ripley B. D., 1988, *Statistical inference for spatial processes*, Cambridge University Press, Cambridge

Rowan-Robinson M., Walker D., Chester T. et al., 1986, MNRAS 219, 273

Schmalzing J., Kerscher M., Buchert T.: 1996, *Minkowski functionals in cosmology*. In: *Proceedings of the international school of physics Enrico Fermi. Course CXXII: Dark matter in the Universe* (Varenna sul Lago di Como), Bonometto, S., Primack, J., Provenzale, A. (eds.), Società Italiana di Fisica, p. 281

Sylos Labini F., Gabrielli A., Montuori M., Pietronero L., 1996, Physica A 226, 195

Sylos Labini F., Pietronero L., Montuori M.: 1997, *Frequently asked questions about fractals*. In: *Proc. 2<sup>nd</sup> SFB workshop on Astro-particle physics Ringberg 1996, Report SFB375/P002* (Ringberg, Tegernsee), Bender, R., Buchert, T., Schneider, P. (eds.), p. 109

van Lieshout M. N. M., Baddeley A. J., 1996, Statist. Neerlandica 50, 344

White S. D. M., 1979, MNRAS 186, 145

Yess C., Shandarin S. F., Fisher K. B., 1997, ApJ 474, 553